Rapid Communications

Spin Seebeck effect in Cu_2OSeO_3: Test of bulk magnon spin current theory

A. Akopyan,[1] N. Prasai,[1,*] B. A. Trump,[2,3,†] G. G. Marcus,[3] T. M. McQueen,[2,3,4] and J. L. Cohn[1,‡]

[1]*Department of Physics, University of Miami, Coral Gables, Florida 33124, USA*

[2]*Department of Chemistry, Johns Hopkins University, Baltimore, Maryland 21218, USA*

[3]*Department of Physics and Astronomy, Institute for Quantum Matter, Johns Hopkins University, Baltimore, Maryland 21218, USA*

[4]*Department of Material Science and Engineering, Johns Hopkins University, Baltimore, Maryland 21218, USA*

(Received 9 December 2019; accepted 24 February 2020; published 23 March 2020)

We report measurements of the low-temperature ($T \leqslant 15$ K) longitudinal spin Seebeck coefficient (S_{LSSE}) in bulk single crystals of the helimagnetic insulator Cu_2OSeO_3 with Pt contacts. Simultaneous measurement of both S_{LSSE} and the magnon thermal conductivity (κ_m) demonstrates their correlation and allows for quantitative and favorable comparison to bulk magnon spin current theory.

DOI: 10.1103/PhysRevB.101.100407

Magnon transport and energy exchange between magnons and phonons are central to the growing fields of spin caloritronics [1] and magnon spintronics [2]. Crucial to potential applications is the conversion of thermally driven spin currents in a magnetic insulator to an electrical signal via the inverse spin Hall effect in a heavy-metal thin film in interfacial contact—the spin Seebeck effect. Considerable experimental and theoretical development has focused on studies of Pt contacts to the insulating ferrimagnet yttrium-iron garnet (YIG).

Magnon spin current theory for the bulk spin Seebeck effect [3–5] implies a direct relationship between the longitudinal spin Seebeck coefficient (S_{LSSE}) and magnon thermal conductivity (κ_m). Quantitative tests of this relationship have not been possible in any material because κ_m is not typically large enough or easily separable from the lattice thermal conductivity. Though κ_m has been determined for YIG at low temperature in applied magnetic field [6–8], it is not clearly correlated with S_{LSSE} (e.g., their maxima appear to occur at very different temperatures [9,10]).

Recent studies [11] demonstrated that Cu_2OSeO_3, a helimagnetic insulator with $T_C = 58$ K, harbors the largest known κ_m for any ferro- or ferrimagnetic insulator, with a maximum $\kappa_m \sim 60$–80 W/mK at $T \simeq 5$–6 K. Here we report on measurements of S_{LSSE} in 10-nm Pt/bulk single-crystal Cu_2OSeO_3 heterostructures with which κ_m, measured simultaneously, is well correlated. The data, which include interfacial spin-mixing conductances varying by more than an order of magnitude, are in quantitative agreement with the predictions of bulk spin current theory.

Cu_2OSeO_3 comprises a three-dimensional distorted pyrochlore (approximately fcc) lattice of corner-sharing Cu tetrahedra [12,13]. Strong magnetic interactions within tetrahedra lead to a 3-up–1-down, spin $S = 1$ magnetic state [14,15] with weaker interactions between tetrahedra leading to their ferromagnetic ordering [16,17] below $T_C \simeq 58$ K. At low temperatures [18] the low-field state [inset, Fig. 1(a)] includes multiple helical (H) domains (aligned along the $\langle 100 \rangle$ easy-axis directions) wherein atomic spins rotate within a plane perpendicular to the helical axis with a wavelength $\lambda_h \simeq 62$ nm. At $H \gtrsim 10$–25 mT (depending on field orientation) the helices of individual domains rotate along the field to form a single-domain, conical phase (C). For $H \gtrsim 50$–75 mT the ferrimagnetic, fully polarized (FP) state emerges.

Phase pure, single crystals of Cu_2OSeO_3 were grown by chemical vapor transport as described elsewhere [11,19]. Specimens were cut from single-crystal ingots, oriented by x-ray diffraction, and polished into thin parallelepipeds. A two-thermometer, one-heater method was employed to measure the spin Seebeck effect (using 25-μm-diam. Au wires) and thermal conductivity simultaneously. A sputtered Pt film (10 nm thick) was deposited onto the heater end of the crystal and isolated from the heater with varnish. Further details on the measurements, crystal polishing/etching [20–21], and properties of the Pt films are discussed in the Supplemental Material [22].

We focus in this work on data for three specimens, all with heat flow along the [111] direction and magnetic field along $[1\bar{1}0]$ [inset, Fig. 1(a)]. Crystal 1 is the same crystal ($5 \times 1.10 \times 0.26$ mm^3) for which thermal conductivity data were reported in Ref. [11]. This crystal was subsequently cut, polished (new cross-sectional area $A = 0.86 \times 0.20$ mm^2), prepared with a fresh Pt film, and remeasured. This second data set is the primary focus of the narrative since it is most extensive and because its SSE signal was a factor of 4–5 larger than during the first experiment. The two specimens are distinguished by their transverse dimensions, $\ell_0 = 0.60$ mm and 0.47 mm, respectively, where $\ell_0 \equiv 2\sqrt{A/\pi}$. A second crystal with $\ell_0 = 0.31$ mm ($A = 0.70 \times 0.11$ mm^2; crystal 5 from Ref. [11]) was also studied. Data for the $\ell_0 = 0.60$ mm and $\ell_0 = 0.31$ mm specimens are included in Fig. 3 and more extensive data in Supplemental Material Figs. S4 and S5 [22].

*Present address: Department of Physics, St. Mary's College of Maryland, St. Mary's City, MD 20686.

†Present address: NIST Center for Neutron Research, National Institute of Standards and Technology, Gaithersburg, Maryland 20899-6102.

‡Corresponding author: jcohn@miami.edu

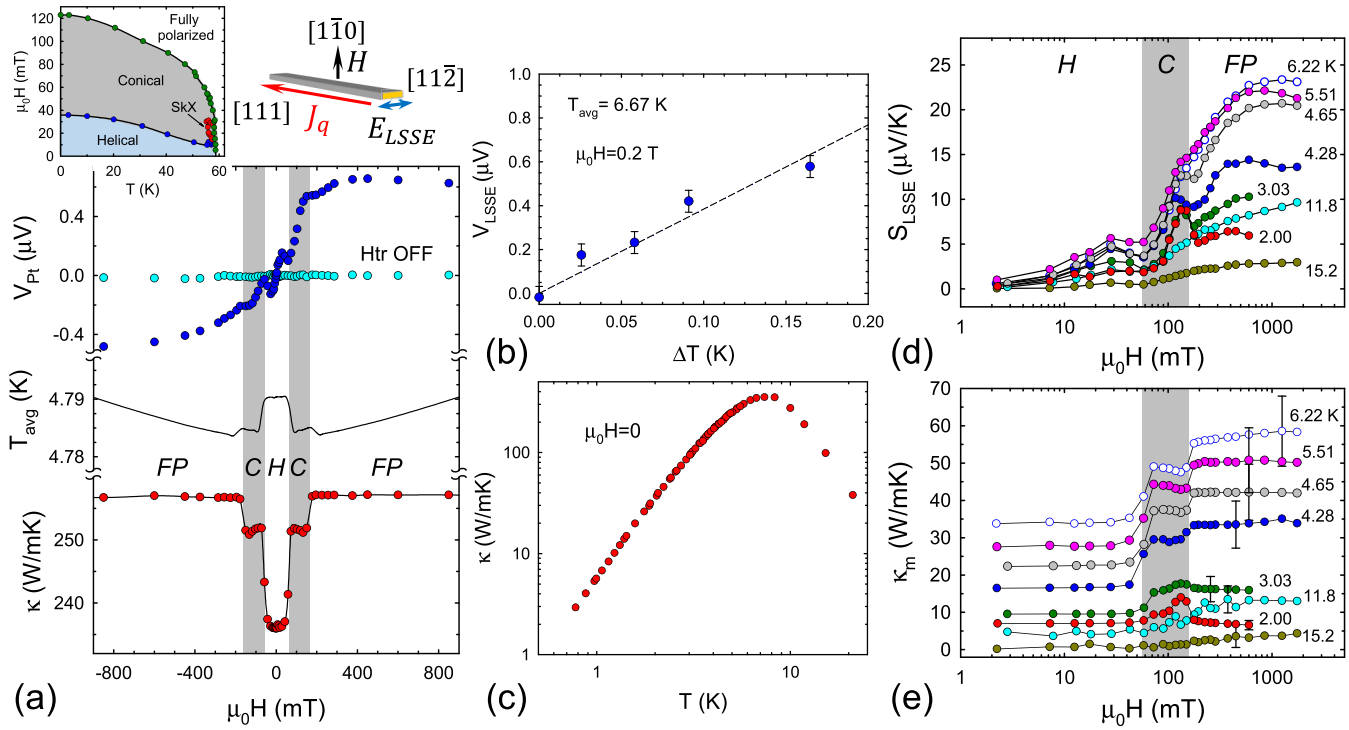

FIG. 1. (a) From top to bottom: Spin Seebeck voltage (for heater on and off), average temperature, and thermal conductivity vs applied field at $T_{\rm avg} = 4.79$ K. Left inset: Magnetic phase diagram (adapted from Ref. [18]); right inset: Orientation of heat flow and fields. (b) SSE voltage vs ΔT at 6.67 K, (c) zero-field $\kappa(T)$, (d) SSE coefficient, and (e) magnon thermal conductivity vs applied field for various temperatures. Error bars are discussed in the text and in Ref. [11]. The shading in (a), (d), and (e) distinguishes the conical (C) spin phase from helical (H) and fully polarized (FP) phases at lower and higher field, respectively.

Given the high thermal conductivity of Cu_2OSeO_3 [11] and the desire to maximize length along the inverse spin Hall field ($[11\bar{2}]$), long, thin parallelepiped specimens were necessary, leading to large demagnetization factors ($N \sim 0.75$) and some nonuniformity of the applied field; we report external field values here. Extensive prior measurements of $M(H)$ and $\kappa(H)$ on crystals [11,23] with small N reveal consistent, coincident signatures of the spin-phase transitions that are employed here to identify the phase boundaries from $\kappa(H)$ data.

Prior work demonstrates that field-dependent changes in κ are entirely magnonic [11,23]. Separation of κ_L and κ_m is possible for $T \lesssim 1.2$ K where the high-field condition $E_H \gg k_B T$ is met ($E_H = g\mu_B H$, the Zeeman energy) and thus spin-wave excitations are depopulated (gapped). The mean free paths for both phonons and magnons are comparable to ℓ_0 at $T \lesssim 2$ K. At higher T where field suppression of κ_m is incomplete, Callaway model fitting is employed to estimate κ_L, with κ_m computed by subtraction [11,22].

Figure 1(a) shows the field dependence of, from top to bottom, the Pt film voltage (with a constant offset voltage subtracted), average specimen temperature, and thermal conductivity at $T_{\rm avg} = 4.79$ K. The null Pt voltage during the same sweep with the heater off is also shown. Figure 1(b) confirms linearity in ΔT of the antisymmetrized spin Seebeck voltage, $V_{LSSE} = [V_{\rm Pt}(H) - V_{\rm Pt}(-H)]/2$, and Fig. 1(c) shows the zero-field $\kappa(T)$. $\kappa(H)$ exhibits a steplike increase at the H-C spin-phase transition, a plateau within the C phase, and another steplike increase at the C-FP phase boundary. Similar features for various orientations of heat flow and applied field have been reported in prior studies [11,23].

Figure 1(d) shows the longitudinal spin Seebeck coefficient as a function of field at selected temperatures, $S_{LSSE} = (V_{LSSE}/\Delta T)(l/w)$, where l is the distance between thermometers along the heat flow and w is the length of the Pt film (approximately the specimen width). Figure 1(e) shows the magnon thermal conductivity computed by subtracting a field-independent κ_L. The error bars reflect uncertainties in estimating κ_L from the model fitting and are largest at $T \sim 7$ K where $\kappa(T)$ has its maximum [11,22]. Similar $S_{LSSE}(H)$ and $\kappa_m(H)$ data for the other specimens are presented in Figs. S4 and S5 [22].

$S_{LSSE}(H)$ exhibits a small maximum at fields below the H-C phase transition, presumably associated with partial reorientation of the three ⟨100⟩-oriented helical domains, established in zero-field cooling. A sharp increase in $S_{LSSE}(H)$ characterizes the transition to the conical phase, following the increase in $\kappa_m(H)$. At $T \gtrsim 6$ K, $S_{LSSE}(H)$ increases smoothly through the C-FP transition, and saturates or declines in magnitude within the FP phase. For lower T an inflection appears at the C-FP transition and a steplike decrease emerges, becoming more prominent at the lowest T. This latter feature coincides with a steplike decrease in $\kappa_m(H)$ (see data for 3.03 and 2.00 K), and thus can be attributed to the effects of a larger spin gap (estimated in the analysis below as $\Delta \sim 0.3$ meV [22]) within the FP phase (the spin gap in the conical phase is quite small [24], ~12 μeV). A fraction of the thermal magnons thus become gapped as the field increases through the C-FP

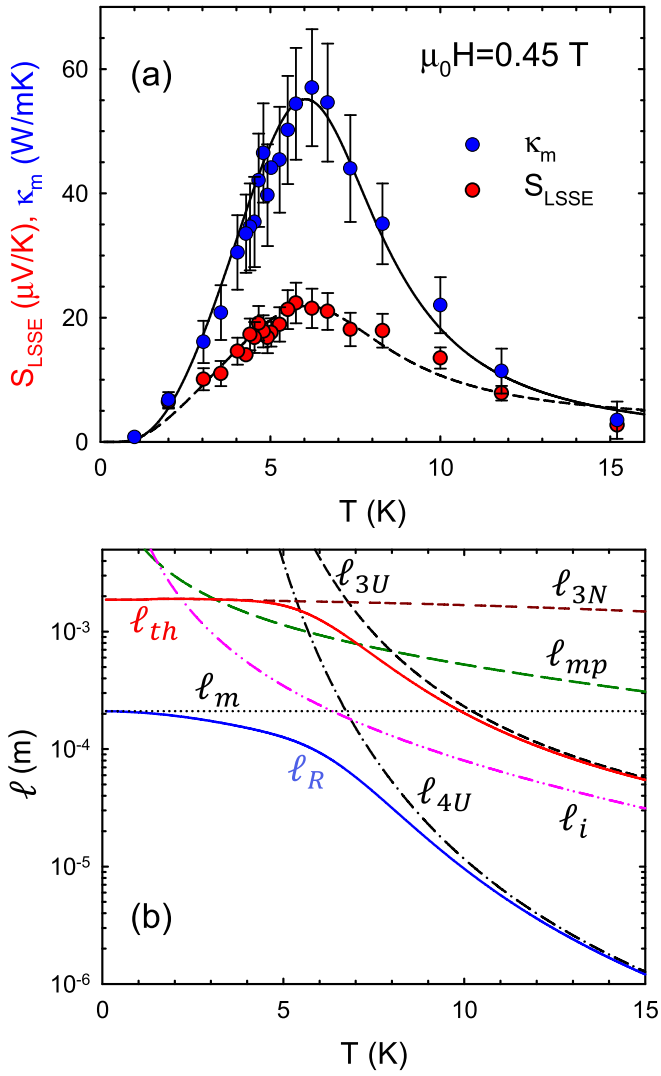

FIG. 2. (a) $\kappa_m(T)$ and $S_{LSSE}(T)$ in the fully polarized phase at $\mu_0 H = 0.45$ T. Error bars for κ_m are described in the text, and for S_{LSSE} are dictated by uncertainty in the geometric factor (20%). The solid curve is computed from Eq. (1) and the dashed curve from Eq. (2) with $\tau_{th} = (\tau_{3N}^{-1} + \tau_{mp}^{-1} + \tau_{3U}^{-1})^{-1}$ (see text). (b) Thermally averaged scattering lengths computed from the model of Ref. [30] (see also the Supplemental Material [22]).

transition, effectively removing their contribution to κ_m. That the effects of the spin gap opening are evidenced in S_{LSSE} at higher T than for κ_m suggests that *subthermal* magnons contribute some weight to the spin Seebeck effect, as has been proposed to understand the field-induced suppression of the SSE in YIG [9,25,26].

The most significant observation from Figs. 1(d) and 1(e) and the principal result of this work, is the clear correspondence between κ_m and S_{LSSE}; Fig. 2(a) illustrates this correspondence in T at fixed field $\mu_0 H = 0.45$ T, within the *FP* phase where S_{LSSE} is near its maximum value. As a first test of theory, we demonstrate that the same magnon relaxation rate, employed in prior work to model $\kappa_m(T)$ for crystal 1 and other similar crystals [11], also describes $S_{LSSE}(T)$.

Inelastic neutron scattering studies [27] indicate a single spin-wave branch relevant to magnon transport at low T in

TABLE I. Magnon scattering and spin Seebeck parameters.

Specimen	ℓ_0 (mm)	c (ppm)	ℓ_m (mm)	R_N (Ω)	$g_{\rm eff}^{\uparrow\downarrow}$ (10^{15} m^{-2})
Crystal 1	0.60	22	0.30	467	2.45
”	0.47	22	0.21	120	39.3
Crystal 2	0.31	44	0.18	293	1.27

Cu_2OSeO_3 that is well described by an isotropic dispersion [28], $E = \Delta + g\mu_B H + \hbar\omega_{ZB}[1 - \cos(\pi q)]$, with $\hbar\omega_{ZB} = 4.55$ meV and $q = k/k_m$ the reduced wave number (k_m is the maximum wave number). The magnon thermal conductivity and spin Seebeck coefficient from Boltzmann theory can be written as [3–5]

$$\kappa_m = \frac{k_B k_m^3}{6\pi^2}\tau_R B_{21}, \tag{1}$$

$$S_{LSSE} = R_N \lambda_N \frac{2e}{\hbar}\theta_{SH}(\tau_m\tau_{th})^{1/2}\frac{B_{11}C_2}{(B_{10}C_1)^{1/2}} F g_{\rm eff}^{\uparrow\downarrow}, \tag{2}$$

where B_{ij} and C_k are the integrals,

$$B_{ij} = \int_0^1 dq\, q^2 v_m^2 \frac{x^i (e^x)^j}{(e^x-1)^{1+j}}, \quad C_k = \int_0^1 dq\, q^2 \frac{x^k}{(e^x-1)},$$

$$F = \frac{\hbar\gamma k_B k_m^3}{4\pi M_S \pi^2\sqrt{3}},$$

$v_m = (1/\hbar)dE/dk$ is the magnon velocity; $x = E/k_BT$; R_N, $\lambda_N = 3.7$ nm and $\theta_{SH} = 0.05$ are the Pt film resistance, spin-diffusion length, and spin Hall angle [5]; $\gamma = 1.82 \times 10^{11}$ T^{-1} s^{-1} is the gyromagnetic ratio [29]; and $4\pi M_S \simeq 1.15 \times 10^5$ A/m is the saturation magnetization [18]. The integrals are performed over a spherical Brillouin zone with $(4/3)\pi k_m^3 = (2\pi/a)^3$. We employ thermally averaged scattering times for which the momentum dependence has already been integrated out.

The transport relaxation rate (τ_R^{-1}) incorporates magnon-magnon umklapp ($3U$, $4U$), magnon-impurity (i), and magnon-boundary (b) scattering, $\tau_R^{-1} = \tau_{3U}^{-1} + \tau_{4U}^{-1} + \tau_i^{-1} + \tau_b^{-1}$, computed for an isotropic Heisenberg model with quadratic magnon dispersion [30]. The expressions rely on four parameters, two of which are fixed by the value of the lattice constant and T_C [11,22]. The strength of impurity and boundary terms are set by the nonmagnetic impurity concentration (c) and magnetic domain size $\ell_m \leqslant \ell_0$ ($\tau_b = \ell_m/\langle v_m\rangle$, with $\langle v_m\rangle$ the momentum-averaged magnon velocity [22]). The latter, employed here as a fitting parameter, was determined directly in Ref. [11] from the $\kappa_m \propto T^2$ behavior observed within the C phase at low T as ~0.30 mm for the specimen with $\ell_0 = 0.60$ mm. The solid curve in Fig. 2(a) demonstrates good agreement with κ_m using the T-dependent scattering lengths ($\ell_j = \langle v_m\rangle\tau_j$) shown in Fig. 2(b). Similar quality fitting curves for the other specimens are shown in Figs. S4 and S5 [22]; Table I summarizes the parameters.

Two relaxation times are distinguished in Eq. (2) for the SSE coefficient, characterizing scattering that conserves (does not conserve) magnon number, τ_m (τ_{th}) [31]; the magnon diffusion length and the SSE signal are proportional to $\sqrt{\tau_m\tau_{th}}$, where $\tau_m \ll \tau_{th}$. We take $\tau_m = \tau_R$, as τ_R is dominated by magnon-conserving processes given that $\tau_{3U} \ll \tau_{4U}$

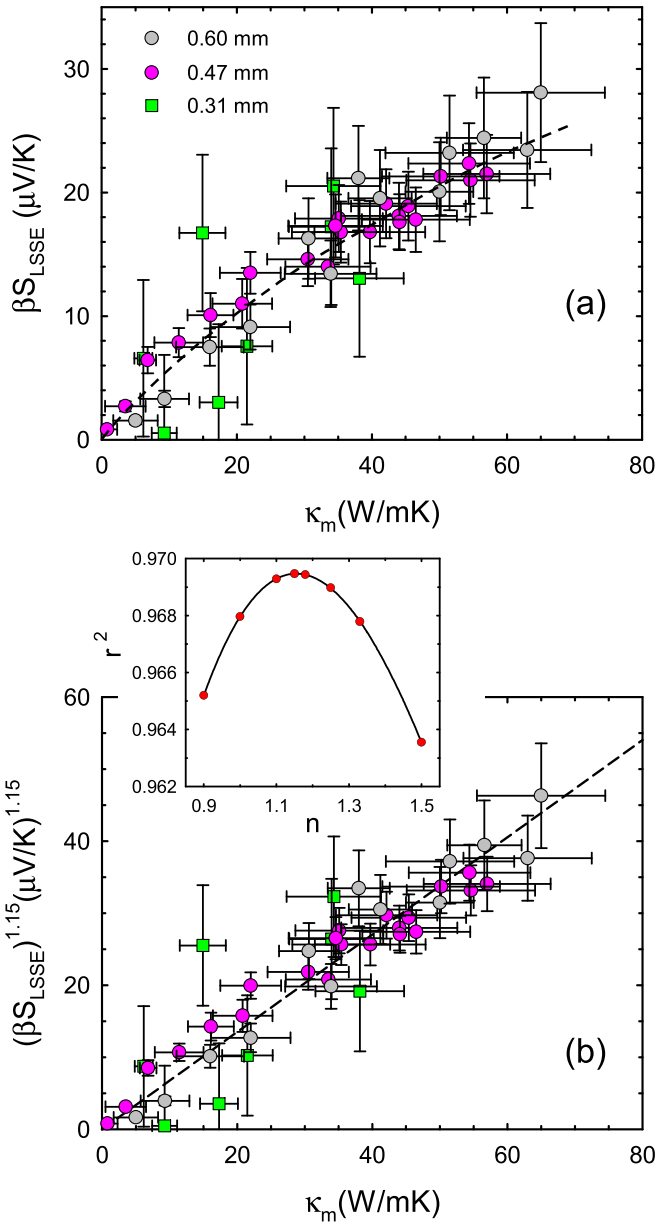

FIG. 3. Correlation between S_{LSSE} and κ_m in the fully polarized phase ($\mu_0 H = 0.45\,\mathrm{T}$) for all three specimens on linear (a) and power-law (b) scaling. Data for crystal 1 with $\ell_0 = 0.60\,\mathrm{mm}$ and crystal 2 ($\ell_0 = 0.31\,\mathrm{mm}$) have been rescaled by their values of $R_N g_{\mathrm{eff}}^{\uparrow\downarrow}$ (Table I) to match that of crystal 1 with $\ell_0 = 0.47\,\mathrm{mm}$ as described in the text. The dashed line in (a) is a guide and in (b) a linear least-squares fit. The inset shows the quality of the power-law fit to be maximized for $n = 1.15$.

[Fig. 2(b)]. Note that magnon-phonon interactions (characterized by τ_{mp}), which do not conserve magnon number (two-magnon, one-phonon interactions are predominant), are weak in the low-T regime relevant here [30,32] and play little role in κ_m provided there is sufficient coupling to ensure energy from the heater (coupling only to phonons) enters the magnon system. The criterion for this [33], $\tau_{mp} \gtrsim \ell_0/v_{ph}$ ($v_{ph} \simeq 2\,\mathrm{km/s}$ is the phonon velocity [11,22]), is satisfied [11] using τ_{mp} estimated from the intrinsic ferromagnetic resonance linewidth [29] [Fig. 2(b)]. With $\tau_m = \tau_R$ fixed by fitting to $\kappa_m(T)$ and $\tau_{th}^{-1} = \tau_{mp}^{-1} + \tau_{3N}^{-1} + \tau_{3U}^{-1}$, $g_{\mathrm{eff}}^{\uparrow\downarrow}$ was adjusted to produce good agreement with S_{LSSE} [dashed curve in Fig. 2(a) and Figs. S4 and S5 for the other specimens].

The T dependence arising from the relaxation times for S_{LSSE} differs from that for κ_m by the factor $(\tau_{th}/\tau_R)^{1/2}$, which is weakly T dependent over the investigated range [Fig. S6(a)]. This observation motivates a more fundamental test of the theory, independent of the relaxation times—Eqs. (1) and (2) predict the two transport coefficients to be directly related through their integral expressions. A *sublinear* relationship between S_{LSSE} and κ_m for all specimens emerges when the spin Seebeck coefficients are rescaled by plotting βS_{LSSE} against κ_m [Fig. 3(a)], where β is the ratio of $R_N g_{\mathrm{eff}}^{\uparrow\downarrow}$ for the $\ell_0 = 0.47\,\mathrm{mm}$ specimen to that for the others: $\beta = 4.1$ (12.7) for $\ell_0 = 0.60$ (0.31) mm specimens. Figure 3(b) demonstrates that a power-law relation, $(S_{LSSE})^n \propto \kappa_m$, provides a good description of the data with $n = 1.15$ providing the best fit [inset, Fig. 3(b)]. In Fig. S6(b) we demonstrate that the integrals follow the relationship $B_{11}C_2/(B_{10}C_1)^{1/2} \propto (B_{21})^{0.852}$ over most of the T range, yielding $n = (1/0.852) \simeq 1.17$ in excellent agreement with the data.

In summary, the unprecedentedly large magnon thermal conductivity of Cu_2OSeO_3 and simultaneous measurement of spin Seebeck coefficient have allowed for new quantitative tests affirming bulk magnon spin current theory. These results highlight this compound as a model system for the study of magnon interactions and their role in the transport of spin and heat.

Work at the University of Miami was supported by the U.S. Department of Energy (DOE), Office of Science, Basic Energy Sciences (BES), under Award No. DE-SC0008607. T.M.M. was supported as part of the Institute for Quantum Matter, an Energy Frontier Research Center funded by the U.S. DOE, Office of Science, BES under Award No. DE-SC0019331. B.A.T. acknowledges the NSF, Division of Materials Research, Solid State Chemistry, CAREER Grant No. DMR-1253562. G.G.M. acknowledges generous support from the NSF-GRFP, Grant No. DGE-1232825.

[1] Stephen R. Boona, Roberto C. Myers, and Joseph P. Heremans, Energy Environ. Sci. **7**, 885 (2014).

[2] A. V. Chumak, V. I. Vasyuchka, A. A. Serga, and B. Hillebrands, Nat. Phys. **11**, 453 (2015).

[3] Steven S.-L. Zhang and S. Zhang, Phys. Rev. Lett. **109**, 096603 (2012); Phys. Rev. B **86**, 214424 (2012).

[4] S. M. Rezende, R. L. Rodríguez-Suárez, R. O. Cunha, A. R. Rodrigues, F. L. A. Machado, G. A. Fonseca Guerra, J. C. Lopez Ortiz, and A. Azevedo, Phys. Rev. B **89**, 014416 (2014).

[5] S. M. Rezende, R. L. Rodríguez-Suárez, R. O. Cunha, J. C. López Ortiz, and A. Azevedo, J. Magn. Magn. Mater. **400**, 171 (2016).

[6] B. Luthi, J. Phys. Chem. Solids **23**, 35 (1962).

[7] R. L. Douglass, Phys. Rev. **129**, 1132 (1963).

[8] S. R. Boona and J. P. Heremans, Phys. Rev. B **90**, 064421 (2014).

[9] H. Jin, S. R. Boona, Z. Yang, R. C. Myers, and J. P. Heremans, Phys. Rev. B **92**, 054436 (2015).

[10] R. Iguchi, Ken-ichi Uchida, S. Daimon, and E. Saitoh, Phys. Rev. B **95**, 174401 (2017).

[11] N. Prasai, B. A. Trump, G. G. Marcus, A. Akopyan, S. X. Huang, T. M. McQueen, and J. L. Cohn, Phys. Rev. B **95**, 224407 (2017).

[12] P. G. Meunier and M. Bertaud, J. Appl. Crystallogr. **9**, 364 (1976).

[13] H. Effenberger and F. Pertlik, Monatsh. Chem. **117**, 887 (1986).

[14] Jan-Willem G. Bos, C. V. Colin, and T. T. M. Palstra, Phys. Rev. B **78**, 094416 (2008).

[15] M. Belesi, I. Rousochatzakis, H. C. Wu, H. Berger, I. V. Shvets, F. Mila, and J. P. Ansermet, Phys. Rev. B **82**, 094422 (2010).

[16] J. Romhányi, J. van den Brink, and I. Rousochatzakis, Phys. Rev. B **90**, 140404(R) (2014).

[17] M. Ozerov, J. Romhányi, M. Belesi, H. Berger, J.-Ph. Ansermet, J. van den Brink, J. Wosnitza, S. A. Zvyagin, and I. Rousochatzakis, Phys. Rev. Lett. **113**, 157205 (2014).

[18] T. Adams, A. Chacon, M. Wagner, A. Bauer, G. Brandl, B. Pedersen, H. Berger, P. Lemmens, and C. Pfleiderer, Phys. Rev. Lett. **108**, 237204 (2012).

[19] J. Panella, B. A. Trump, G. G. Marcus, and T. M. McQueen, Cryst. Growth Des. **17**, 4944 (2017).

[20] A. Aqeel, N. Vlietstra, A. Roy, M. Mostovoy, B. J. van Wees, and T. T. M. Palstra, Phys. Rev. B **94**, 134418 (2016).

[21] M. B. Jungfleisch, V. Lauer, R. Neb, A. V. Chumak, and B. Hillebrands, Appl. Phys. Lett. **103**, 022411 (2013); S. Pütter, S. Geprägs, R. Schlitz, M. Althammer, A. Erb, R. Gross, and S. T. B. Goennenwein, *ibid.* **110**, 012403 (2017).

[22] See Supplemental Material at http://link.aps.org/supplemental/10.1103/PhysRevB.101.100407 for additional details regarding specimen preparation, data for other specimens, and analysis, which includes Refs. [34–39].

[23] N. Prasai, A. Akopyan, B. A. Trump, G. G. Marcus, S. X. Huang, T. M. McQueen, and J. L. Cohn, Phys. Rev. B **99**, 020403(R) (2019).

[24] M. I. Kobets, K. G. Dergachev, E. N. Khatsko, A. I. Rykova, P. Lemmens, D. Wulferding, and H. Berger, Low Temp. Phys. **36**, 176 (2010).

[25] T. Kikkawa, Ken-ichi Uchida, S. Daimon, Zhiyong Qiu, Y. Shiomi, and E. Saitoh, Phys. Rev. B **92**, 064413 (2015).

[26] I. Diniz and A. T. Costa, New J. Phys. **18**, 052002 (2016).

[27] P. Y. Portnichenko, J. Romhányi, Y. A. Onykiienko, A. Henschel, M. Schmidt, A. S. Cameron, M. A. Surmach, J. A. Lim, J. T. Park, A. Schneidewind, D. L. Abernathy, H. Rosner, J. van den Brink, and D. S. Inosov, Nat. Commun. **7**, 10725 (2016).

[28] Helimagnon excitations influence only the very low energy dispersion, corresponding to wave numbers ($k < k_h = 2\pi/\lambda_h \simeq 0.01$ Å^{-1}) and energies far below those of the thermal magnons relevant to the present experiments (see Ref. [27]). Furthermore, our analysis pertains to data within the fully polarized, collinear magnetic state where helimagnetic effects are absent.

[29] S. Seki, Y. Okamura, K. Kondou, K. Shibata, M. Kubota, R. Takagi, F. Kagawa, M. Kawasaki, G. Tatara, Y. Otani, and Y. Tokura, Phys. Rev. B **93**, 235131 (2016).

[30] J.-J. Forney and J. Jäckle, Phys. Kondens. Materie **16**, 147 (1973).

[31] L. J. Cornelissen, K. J. H. Peters, G. E. W. Bauer, R. A. Duine, and B. J. van Wees, Phys. Rev. B **94**, 014412 (2016).

[32] A. I. Akhiezer, V. G. Bar'yakhtar, and M. I. Kaganov, Sov. Phys. Usp. **3**, 661 (1961).

[33] D. J. Sanders and D. Walton, Phys. Rev. B **15**, 1489 (1977).

[34] S. Y. Huang, X. Fan, D. Qu, Y. P. Chen, W. G. Wang, J. Wu, T. Y. Chen, J. Q. Xiao, and C. L. Chien, Phys. Rev. Lett. **109**, 107204 (2012); Y. M. Lu, Y. Choi, C. M. Ortega, X. M. Cheng, J. W. Cai, S. Y. Huang, L. Sun, and C. L. Chien, *ibid.* **110**, 147207 (2013).

[35] Y. Shiomi, T. Ohtani, S. Iguchi, T. Sasaki, Z. Qiu, H. Nakayama, K. Uchida, and E. Saitoh, Appl. Phys. Lett. **104**, 242406 (2014).

[36] See, e.g., N. Giordano and M. A. Pennington, Phys. Rev. B **47**, 9693 (1993), and references therein.

[37] H. Hoffmann, F. Hofmann, and W. Schoepe, Phys. Rev. B **25**, 5563 (1982).

[38] R. Berman, *Thermal Conduction in Solids* (Oxford University Press, Oxford, 1976).

[39] P. B. Allen, Phys. Rev. B **88**, 144302 (2013).

Supplementary Material for: Spin-Seebeck Effect in Cu_2OSeO_3: Test of Bulk Magnon Spin-Current Theory

A. Akopyan, N. Prasai, B. A. Trump, G. G. Marcus, T. M. McQueen, and J. L. Cohn

PT FILM DEPOSITION AND PROPERTIES

Following the work of Aqeel *et* al. [20], Cu_2OSeO_3 crystal faces were prepared for Pt deposition by polishing with a sequence of increasingly fine abrasive pads: 5 μm, 1 μm, 0.3 μm. Prior to placement in the vacuum chamber for sputter deposition of Pt through a shadow mask, polished surfaces were subjected to a short-duration Piranha etch (a 3:1 ratio of H_2SO_4 with H_2O_2), established as improving the Pt/yttrium-iron-garnet (YIG) interface for spin-pumping applications [21], followed by deionized water rinse. The etching time for the three specimens of this work were: 10 s ($\ell_0 = 0.47$ mm), 45 s ($\ell_0 = 0.60$ mm), 60 s ($\ell_0 = 0.31$ mm). Subsequent to deposition, the films/crystals were annealed in air at 300°C for 20-30 minutes during which their resistances initially decreased and eventually stabilized.

Given that bulk Pt is close to a magnetic instability and ultrathin Pt films deposited on YIG substrates have been shown to develop magnetism [34, 35] (e.g. in a dead layer near the interface), it is important to characterize all Pt films grown on Cu_2OSeO_3 to establish whether there could be extrinsic contributions to SSE measurements. Figure S1 (a) shows low-T measurements of the logarithmic-in-T resistance rise observed at H=0 in several of our Pt films grown on polished Cu_2OSeO_3 crystal surfaces for SSE measurements. The behavior is typical of two-dimensional (2D) thin films where the resistance rise is dictated by weak localization and electron-electron interaction effects [36]. The logarithmic temperature derivative [dashed lines, Fig. S1 (a)] should scale with the sheet resistance (a measure of the disorder in 2D) according to theory,

$$\frac{\Delta R}{R} = -\frac{e^2}{2\pi^2\hbar} R_{\square}(T_0)\alpha_T \ln(T/T_0), \tag{1}$$

where $R_{\square}$ is the sheet resistance, T_0 is a reference temperature [taken to be the temperature of the resistance minimum in Fig. S1 (a)], and α_T is a material constant determined by the strength of weak localization and interaction effects [36]. The value of $\alpha_T \approx 1$ for our films [Fig. S1 (b)] is in excellent agreement with the established value [37] for Pt films from the 1980's, $\alpha_T = 1.01 \pm 0.07$.

The films also exhibit Hall resistivities [Fig. S1 (c)] that are linear-in-field with slopes passing through the origin – the absence of an offset that is the signature of an anomalous Hall effect associated with magnetism indicates that the interface magnetism observed in some cases for Pt/YIG interfaces is absent for Pt/Cu_2OSeO_3 heterostructures.

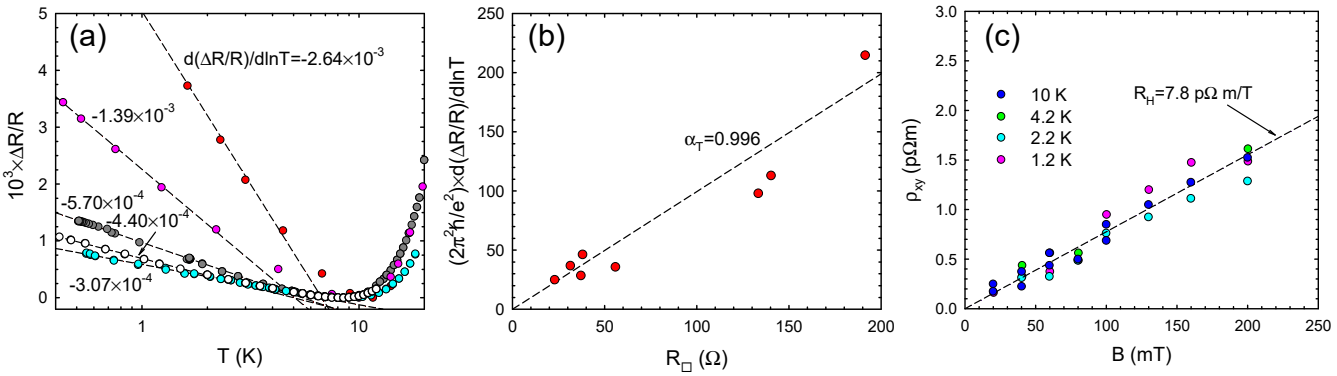

FIG. S1. (a) low-T logarithmic-in-T resistance increase for 5 Pt films deposited on Cu_2OSeO_3 crystals, (b) scaling of $\ln T$ resistance rise with sheet resistance, (c) linear-in-field Hall resistivity for one of the films at low temperature.

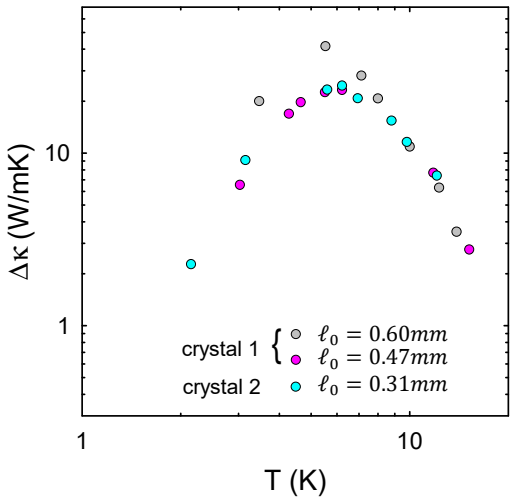

FIG. S2. $\Delta\kappa \equiv \kappa(0.45\mathrm{T}) - \kappa(0)$ *vs.* T for the three crystals from this study.

CALCULATIONS TO ESTIMATE κ_L

Details of the analysis to estimate the lattice thermal conductivity of crystal 1 and other similar Cu_2OSeO_3 crystals were presented in Ref. [11]. For convenience we include those details here. The Callaway model [38], incorporating its recent update [39], was employed to compute $\kappa_L(T)$ for each of the crystals, with parameter ranges restricted by the following constraints: (1) κ_L fits the low-T, high-field data (where κ_L is inferred directly) and the $T \geq 15$ K, zero-field data (where κ_m is inferred to be negligible by the vanishing of $\Delta\kappa \equiv \kappa(0.45\mathrm{T}) - \kappa(0)$, Fig. S2) and (2) the maximum in κ_m, computed by subtracting κ_L from κ measured in the fully-polarized phase, should occur at $T \approx 5-6$ K where $\Delta\kappa$ has its maximum (Fig. S2). The integral expression for κ_L is,

$$\kappa_L = \frac{k_B}{2\pi^2 v}\left(\frac{k_B}{\hbar}\right)^3 T^3 \left[\int_0^{\Theta_D/T} \frac{x^4 e^x}{\left(e^x-1\right)^2}\tau_C(x,T)dx\right]\left(1+\frac{\overline{\tau_C(x,T)/\tau_N(x,T)}}{\overline{\tau_C(x,T)/\tau_R(x,T)}}\right),$$

$$\text{with} \quad \overline{f(T)} = \int_0^{\Theta_D/T} \frac{x^4 e^x}{\left(e^x-1\right)^2} f(x,T)dx \Bigg/ \int_0^{\Theta_D/T} \frac{x^4 e^x}{\left(e^x-1\right)^2}dx,$$

where v is the Debye averaged sound velocity (see above), $\Theta_D = (\hbar v/k_B)(6\pi^2 N/V)^{1/3}$ the Debye temperature, $x = \hbar\omega/k_B T$ the reduced phonon energy, $\tau_C^{-1}(x,T) = \tau_N^{-1}(x,T) + \tau_R^{-1}(x,T)$, and $\tau_N^{-1}(x,T)$ and $\tau_R^{-1}(x,T)$ are phonon scattering rates for normal (momentum conserving) and resistive (momentum non-conserving) processes, respectively. $\tau_R^{-1}(x,T)$ included terms for scattering from boundaries, other phonons (Umklapp scattering), and point-like defects (Rayleigh),

$$\tau_R^{-1}(x,T) = v/\ell_{ph} + Ax^2T^4 \exp\left(-\frac{\Theta_D}{bT}\right) + Cx^4T^4,$$

where $\ell_{ph} = \ell_0$ is the boundary-limited phonon mean-free path and A, b, C are constants. The normal scattering rate was taken to have the same frequency dependence as for Umklapp scattering [39], but without the exponential T dependency, $\tau_N^{-1}(x,T) = \gamma Ax^2T^4$, with γ a dimensionless constant.

Fig. S3 shows $\kappa(H=0,T)$ data for crystal 1 (with $\ell_0 = 0.60$ mm) and crystal 2, along with two κ_L curves for each (solid and dash-dotted curves). These curves border shaded ranges defined by the constraints noted above. The κ_L fits for crystal 1 with $\ell_0 = 0.47$ mm used the same parameters as the curves for $\ell_0 = 0.60$ mm, but with $\ell_{ph} = 0.47$ mm. The values of κ_L used in subtraction to determine κ_m [Fig.'s 1 (e), S4 (b), S5 (b)] correspond to the average of the solid and dash-dotted curves, with error bars determined by the width of the shaded region.

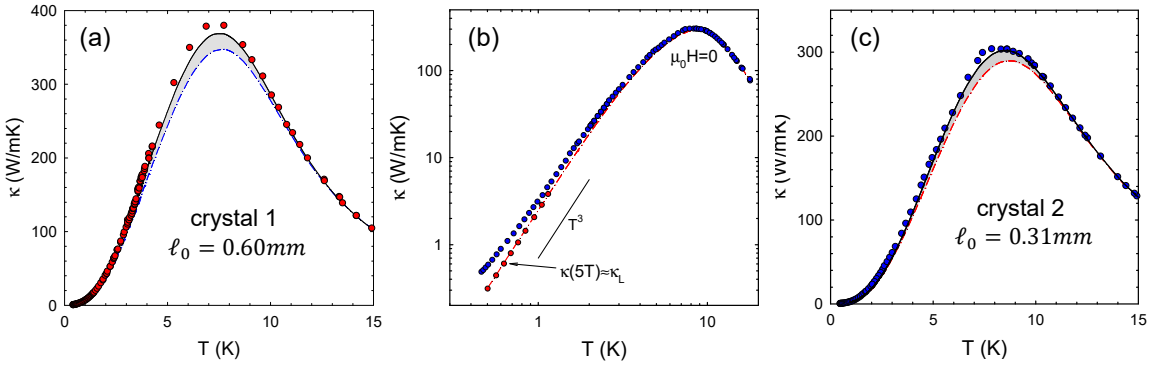

FIG. S3. (a) Zero-field thermal conductivity for crystal 1 ($\ell_0 = 0.60$ mm), and crystal 2 ($\ell_0 = 0.31$ mm) on (b) log-log and (c) linear scaling (blue circles). Also shown in (b) are $\kappa(5T) \approx \kappa_L$ (red circles). Callaway-model calculations for different parameter sets are represented by solid and dashed-dotted curves with the shaded region between them a measure of the uncertainty in κ_L reflected in the error bars for κ_m in Fig.'s 1-3, S4, S5. The solid (dash-dotted) curves in (a) used: $v = 2.06$ (2.15) km/s, $A = 1.87$ (1.77) $\times 10^4$ K^{-4}, $b = 6.35$ (6.6), $C = 36$ (37) K^{-4}, $\gamma = 1/100$ (1/100); The solid (dash-dotted) curves in (c) used: $v = 2.35$ (2.35) km/s, $A = 1.47$ (1.62) $\times 10^4$ K^{-4}, $b = 6.6$ (6.4), $C = 23.6$ (28) K^{-4}, $\gamma = 1/30$ (1/50).

MAGNON SCATTERING RATES

Forney and Jäckle [27] computed the thermally averaged 3-magnon and 4-magnon normal ($3N$, $4N$) and umklapp ($3U$, $4U$) scattering rates and magnon-impurity scattering rate (i) for a quadratic magnon dispersion within the Born approximation, valid for small impurity concentration and $T \ll T_C$:

$$\tau_{3N}^{-1} = 2.6S\frac{k_B}{\hbar}T_d^2 T_e^{-3/2}T^{1/2}, \qquad \tau_{4N}^{-1} = 6.1\times 10^{-4}\frac{k_B T^4}{S^2\hbar T_e^3},$$

$$\tau_{3U}^{-1} = 1.4\times 10^3\frac{Sk_B T_d^2}{\hbar(T_e T)^{1/2}}\exp\left(-12T_e/T\right), \qquad \tau_{4U}^{-1} = \frac{2}{S^2}\frac{k_B T^{3/2}}{\hbar T_e^{1/2}}\exp\left(-12T_e/T\right), \qquad \tau_i^{-1} = 0.4c\frac{k_B}{\hbar}\frac{k_B T^{5/2}}{T_e^{3/2}},$$

where

$$T_d = \frac{(g\mu_B)^2}{k_B a^3}, \qquad T_e = \frac{2SJ}{k_B}.$$

As described in our prior work [11], we initially re-scaled the values $T_d = 0.012$ K and $T_e = 1.0$ K employed in Ref. [27] for EuS ($T_C = 16.5$ K) using the ratio of lattice constants and T_C (as a surrogate for J). These gave $T_d = 0.004$ K and $T_e = 3.5$ K. Subsequently we settled on $T_e = 4.2$ K which provided better agreement with the data. The scattering rates were adopted without modification with the exception of the Umklapp rate prefactors. τ_{4U}^{-1} was decreased by a factor 45 so as to produce better agreement with the maxima in κ_m at $T \sim 5-6$ K. τ_{3U}^{-1} was increased by a factor 5 to produce a stronger T dependence of τ_{th} that yielded better agreement with the S_{LSSE} data at $T \gtrsim 10$ K. With these modifications, the only remaining adjustable parameters for the three specimens were the impurity concentration (c) and the magnon domain size (ℓ_m), where $\tau_b^{-1} = \ell_m/\langle v_m\rangle$, and the thermally averaged magnon velocity is,

$$\langle v_m\rangle \equiv \frac{\pi\omega_{ZB}}{2q_m}\int_0^1 dqq^2 v_m\frac{xe^x}{(e^x-1)^2}\Bigg/\int_0^1 dqq^2\frac{xe^x}{(e^x-1)^2}.$$

As noted in the main text, a small spin gap $\Delta = 0.3$ meV was included in the dispersion because it substantially improved agreement with κ_m and S_{LSSE} on the low-T side of their maxima.

DATA FOR OTHER SPECIMENS

Figure S4 and S5 show data sets for the other two crystals (with $\ell_0 = 0.60$ and 0.31 mm) for which some data is presented in Fig. 3.

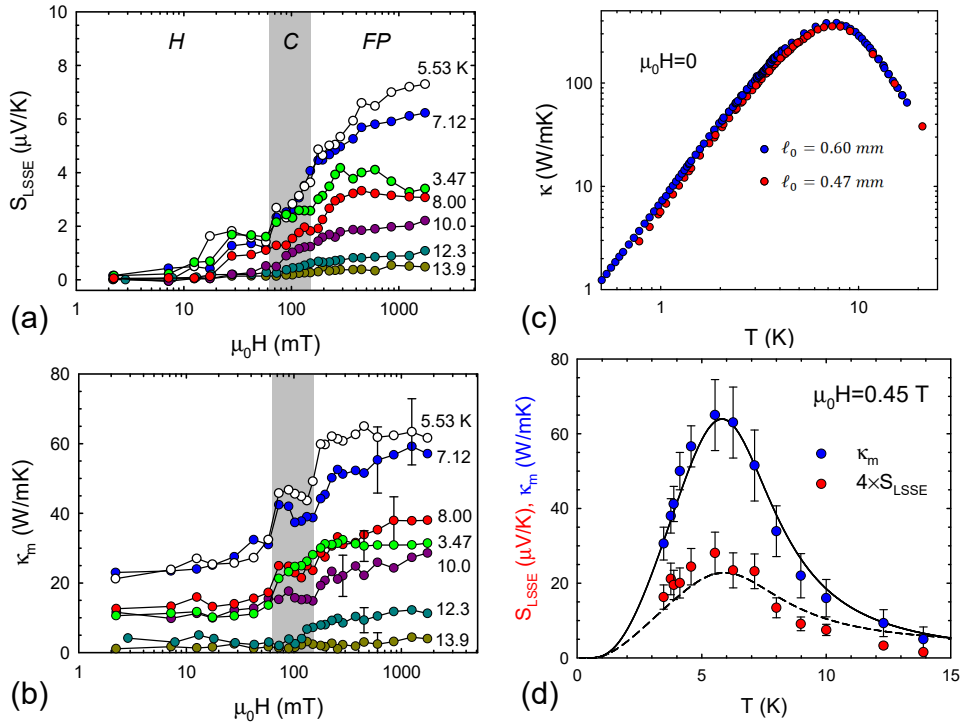

FIG. S4. (a) SSE coefficient and (b) magnon thermal conductivity *vs.* applied field for various temperatures for crystal 1 with $\ell_0 = 0.60$ mm. Error bars are discussed in the main text, in the caption of Fig. S3, and in Ref. 11. The shading distinguishes the conical (C) spin phase from helical (H) and fully-polarized (FP) phases at lower and higher field, respectively. (c) zero-field $\kappa(T)$ for this crystal with different dimensions. (d) Temperature dependence of the spin-Seebeck coefficient and magnon thermal conductivity in the fully-polarized phase at $\mu_0 H = 0.45$ T. Solid and dashed curves were produced using Eq.'s (1) and (2) with parameters listed in Table 1.

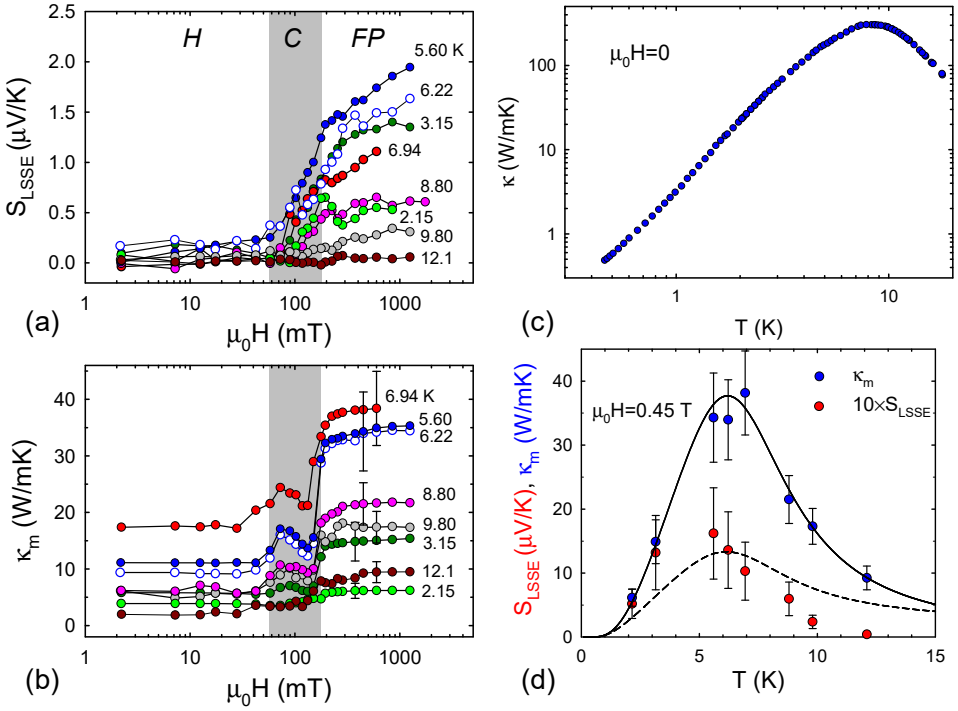

FIG. S5. (a) SSE coefficient and (b) magnon thermal conductivity *vs.* applied field for various temperatures for crystal 2 with $\ell_0 = 0.31$ mm. Error bars are discussed in the main text, in the caption of Fig. S3, and in Ref. 11. The shading distinguishes the conical (C) spin phase from helical (H) and fully-polarized (FP) phases at lower and higher field, respectively. (c) zero-field $\kappa(T)$ comparing both specimens. (d) Temperature dependence of the spin-Seebeck coefficient and magnon thermal conductivity in the fully-polarized phase at $\mu_0 H = 0.45$ T. Solid and dashed curves were produced using Eq.'s (1) and (2) with parameters listed in Table 1.

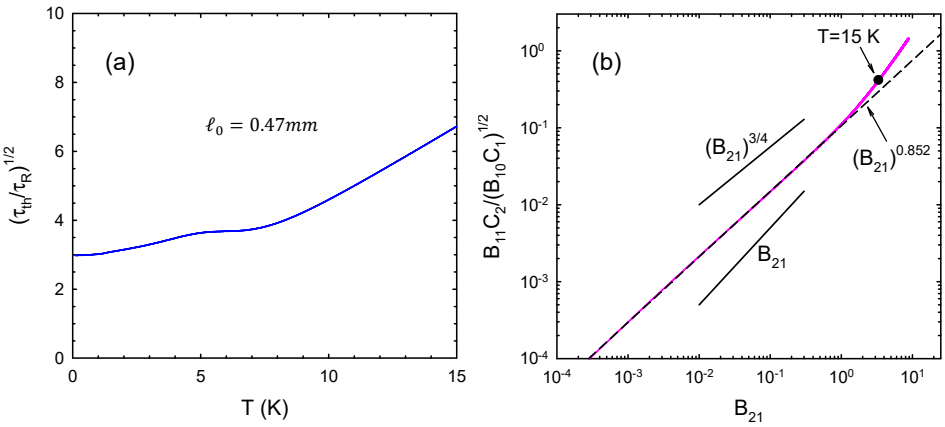

FIG. S6. (a) $(\tau_{th}/\tau_R)^{1/2} = (\ell_{th}/\ell_R)^{1/2}$ *vs.* T using ℓ_{th} and ℓ_R from Fig. 2 (b) employed to fit the κ_m and S_{LSSE} data in Fig. 2 (a). Integrals for S_{LSSE} from Eq. (2) plotted against the κ_m integral from Eq. (1). Axes are scaled so that the maximum of the experimental T range (15K) corresponds to the data point indicated by the arrow.

RELATIONSHIP BETWEEN S_{LSSE} AND κ_m

Figure S6 (a) shows the relatively weak T dependence of the relaxation-time factor $(\tau_{th}/\tau_R)^{1/2}$ that distinguishes S_{LSSE} from κ_m. Figure S6 (b) demonstrates the power-law relationship between the integrals in Eq.'s (1) and (2) defining κ_m and S_{LSSE} (the scaling is adjusted so that $T = 15$ K corresponds to the data point indicated). The inverse of this exponent, $n = 1/0.852 \simeq 1.17$, defines the relationship $(S_{LSSE})^n \propto \kappa_m$ described in Fig. 3.

[34] S. Y. Huang, X. Fan, D. Qu, Y. P. Chen, W. G. Wang, J. Wu, T. Y. Chen, J. Q. Xiao, and C. L. Chien Phys. Rev. Lett. **109**, 107204 (2012); Y. M. Lu, Y. Choi, C. M. Ortega, X. M. Cheng, J.W. Cai, S.Y. Huang, L. Sun, and C. L. Chien, *ibid.* **110**, 147207 (2013).

[35] Y. Shiomi, T. Ohtani, S. Iguchi, T. Sasaki, Z. Qiu, H. Nakayama, K. Uchida, and E. Saitoh, Appl. Phys. Lett. **104**, 242406 (2014).

[36] See, e.g. N. Giordano and M. A. Pennington, Phys. Rev. B **47**, 96935 (1993), and references therein.

[37] H. Hoffmann, F. Hofmann, and W. Schoepe, Phys. Rev. B **25**, 5563 (1982).

[38] R. Berman, *Thermal Conduction in Solids* (Oxford University Press, Oxford, 1976).

[39] P. B. Allen, Phys. Rev. B **88**, 144302 (2013).